A Lagrangian approach to droplet condensation in atmospheric clouds

Ryan S. R. Sidin,[1] Rutger H. A. IJzermans,[2] and Michael W. Reeks[2]
[1]*Department of Mechanical Engineering, University of Twente, P.O. Box 217, 7500 AE Enschede, The Netherlands*
[2]*School of Mechanical and Systems Engineering, Newcastle University, Stephenson Building, Newcastle-upon-Tyne NE1 7RU, United Kingdom*

(Received 24 February 2009; accepted 19 August 2009; published online 23 October 2009)

The condensation of microdroplets in model systems, reminiscent of atmospheric clouds, is investigated numerically and analytically. Droplets have been followed through a synthetic turbulent flow field composed of 200 random Fourier modes, with wave numbers ranging from the integral scales [$\mathcal{O}(10^2$ m)] to the Kolmogorov scales [$\mathcal{O}(10^{-3}$ m)]. As the influence of all turbulence scales is investigated, direct numerical simulation is not practicable, making kinematic simulation the only viable alternative. Two fully Lagrangian droplet growth models are proposed: a one-way coupled model in which only adiabatic cooling of a rising air parcel is considered, and a two-way coupled model which also accounts for the effects of local vapor depletion and latent heat release. The simulations with the simplified model show that the droplet size distribution becomes broader in the course of time and resembles a Gaussian distribution. This result is supported by a theoretical analysis which relates the droplet surface-area distribution to the dispersion of droplets in the turbulent flow. Although the droplet growth is stabilized by vapor depletion and latent heat release in the two-way coupled model, the calculated droplet size distributions are still very broad. The present results may provide an explanation for the rapid growth of droplets in the coalescence stage of rain formation, as broad size distributions are likely to lead to enhanced collision rates between droplets. © *2009 American Institute of Physics*. [doi:10.1063/1.3244646]

I. INTRODUCTION

Despite the familiarity of the phenomenon, the development of rain showers is not yet completely understood, and therefore subject to many studies (see, e.g., Ref. 1 and references therein). In general terms, three stages can be distinguished in the process of rain drop formation. First, droplets are generated by heterogeneous nucleation of water vapor on submicron sized aerosols which act as cloud condensation nuclei (CCNs). Although it has been speculated that very large condensation nuclei may exist in a cloud,[2,3] it is generally believed that CCNs have a size of the order of $r_d=0.1$ μm (Refs. 4–6) so that droplets start off at submicron sizes. If the conditions allow, the droplets grow to a diameter of millimeters in a subsequent stage. Finally, the droplets are large enough to fall, under the influence of gravity, through the cloud and reach the ground.

The growth process of droplets from submicron scales to millimeter scales is due to condensation (i.e., impingement of vapor molecules onto a droplet) and due to coalescence between droplets. While the condensation process depends mainly on local thermodynamic quantities such as temperature and supersaturation, the coalescence process is related to the inertia of droplets or to the occurrence of Brownian and/or turbulent aggregation.

The effect of inertia is manifested in three phenomena: (i) turbulence-induced preferential concentration of droplets,[7–9] (ii) decorrelation between velocities of nearby droplets ("caustics"[10]), and (iii) gravitational settling with large droplets overtaking and collecting smaller ones.[11,12] In order to estimate for which of the droplet sizes, inertia-induced coalescence is important, it is instructive to look at the Stokes number St, a measure for the droplet's inertia compared to the smallest scales of turbulence.[13] Here, it is conveniently expressed as

$$\mathrm{St}=\frac{2}{9}\left(\frac{\rho_d}{\rho_{\mathrm{mix}}}\right)\left(\frac{r_d}{\eta_k}\right)^2, \tag{1}$$

where ρ_d denotes the bulk density of the water droplet, r_d is the droplet radius, ρ_{mix} is the density of the surrounding mixture of vapor and air, and η_k is the Kolmogorov length scale. In atmospheric clouds, typical values of the Kolmogorov length, velocity, and time scales are $\eta_k=10^{-3}$ m, $v_k=0.025$ m/s, and $\tau_k=0.04$ s,[5] respectively. Hence, for droplets of size 10 μm and a typical density ratio of $\rho_d/\rho_{\mathrm{mix}}=10^3$, the Stokes number is approximately 0.02. The settling velocity v_s of these droplets in still air under the action of gravity (with acceleration $g=9.81$ m/s^2) is $v_s=\mathrm{St}\,\tau_k g=0.008$ m/s, which is considerably smaller than the Kolmogorov velocity scale. Therefore, droplets with radius smaller than ~ 10 μm can be expected to closely follow the turbulent flow in an atmospheric cloud, whereas inertia effects become important only for larger droplets.

From the above discussion it is clear that Brownian aggregation, turbulent aggregation, and/or condensation are the remaining mechanisms responsible for the initial growth of droplets with radii between 10^{-7} and 10^{-5} m. For Brownian or turbulent aggregation, the rate of droplet interception is proportional with the volume fraction of droplets.[5] With an interdroplet separation distance of 10^{-3} m typically observed for atmospheric clouds,[5] and assuming a mean droplet radius

of 10^{-5} m, the volume fraction associated with the dispersed droplets is $\sim 10^{-6} \ll 1$. Thus, the corresponding rate of aggregation is very small, and therefore, it is concluded that condensation must be the dominant mechanism, which is responsible for the initial growth of droplets of radii between 10^{-7} and 10^{-5} m.

To predict the variation in droplet size in the inertia-induced coalescence stage of growth, a reliable and accurate description of the droplet size distribution at the onset of this stage is necessary. In particular, the broadness of the size distribution may have a profound influence on the coalescence rate of droplets, and thus on the time scales involved in the initiation of rain. Indeed, Bec *et al.*[14] found that the collision rates in a turbulent flow between polydisperse droplets can be considerably higher than between monodisperse droplets. This is our main motivation to investigate the evolution of the droplet size distribution during the process of condensation in atmospheric clouds.

One of the first theoretical studies on droplet condensation in clouds was published by Twomey[15] in 1959. His theory is based on the assumption that a group of droplets may rise through a cloud in a parcel of air and remain together for a long time. The growth law of each droplet in the parcel can be approximated by $dr_d/dt = \tilde{G}s/r_d$, where $\tilde{G}$ is a constant and s is the local supersaturation.[1] As the growth rate is inversely proportional to r_d, small droplets grow faster than large droplets, and therefore, the droplet size distribution is expected to become narrower as the mean droplet radius increases. However, this prediction is not in agreement with experimental evidence, which suggests that the droplet size distributions in atmospheric clouds are broad even when the droplets are of micrometer sizes (see, e.g., Refs. 2 and 16).

In recent years, a number of theoretical and numerical studies on condensation in atmospheric clouds have also been conducted. Vaillancourt *et al.*[17,18] carried out a direct numerical simulation (DNS) of condensation in a turbulent flow, thereby including various physical phenomena relevant for atmospheric clouds. However, due to the relatively small sizes of the computational domains used, they observed only a marginal spreading of the droplet size distribution in Ref. 18. Celani *et al.*[19,20] used a more simplified theoretical model, which is a generalization of Twomey's condensation model[15] and includes an approximation of the spatiotemporal evolution of the temperature and supersaturation fields in actual atmospheric clouds. Using two-dimensional DNS, they solved an energy balance for the temperature field and a liquid-vapor mass balance for the supersaturation field simultaneously with the Navier–Stokes equations, while tracking the condensing droplets in Lagrangian fashion. By employing this Eulerian–Lagrangian model, they were able to show that significant spreading of the droplet size distribution may take place, with the largest droplets situated in regions where the supersaturation is the highest. Similar results were reported in a more recent investigation by Lanotte *et al.*,[21] in which a three-dimensional DNS was carried out, using a model similar to the one employed by Celani *et al.* in Ref. 19.

All these numerical simulations are understandably restricted by computational limitations since real atmospheric clouds are associated with excessively large values of the Reynolds number and large separations of length scales. For example, performing a DNS of the turbulent flow in a cloud with an integral length scale $L_0 = 100$ m and Kolmogorov length scale $\eta_k = 10^{-3}$ m would require at least $(L_0/\eta_k)^3 = 10^{15}$ grid cells, with billions of droplets that need to be traced. Such requirements are evidently beyond the capabilities of modern computers. In order to circumvent this problem, Vaillancourt *et al.*[18] focused on the smallest scales of turbulence and chose a calculation domain of $(0.1\ \text{m})^3$. Celani *et al.*[20] on the other hand did include the largest scales in their DNS of turbulence, but they were not able to resolve the smallest scales, despite the two-dimensionality of their model. The DNS carried out by Lanotte *et al.*[21] provides a near full resolution of the smallest scales [$\mathcal{O}(1\ \text{mm})$], but the largest scales considered are less than 1 m. They recover the results for actual cloud sizes [$\mathcal{O}(100\ \text{m})$] by extrapolating their DNS results, using a scaling law involving the microscale Reynolds number.

The basic physics of the role played by turbulence in the broadening of the droplet size distribution is described by Celani *et al.* in Ref. 19. They point out that (i) large-scale motions can transport individual droplets over large variations in altitude, which results in different droplet sizes for different droplet trajectories, and that (ii) small-scale turbulent fluctuations can mix droplets of different sizes. Both phenomena together result in a broad droplet size distribution *locally*, which is essential for the coalescence mechanism to be enhanced.

In the present paper, we propose a fully Lagrangian numerical approach to investigate the condensation of droplets in a model system, reminiscent of atmospheric clouds. This allows us to carry out a three-dimensional numerical simulation in which all relevant scales of turbulent motion are taken into account: from the integral scales [$\mathcal{O}(10^2\ \text{m})$] down to the Kolmogorov scales [$\mathcal{O}(10^{-3}\ \text{m})$]. By assuming the turbulence to be homogeneous, isotropic, and statistically stationary, we model the velocity field by a kinematic simulation composed of 200 random Fourier modes. In this flow, the trajectories of a limited number of individual droplets, contained inside a small sampling space, are calculated *backward in time* in order to determine their past trajectories. Subsequently, the size of each droplet along its trajectory is then calculated *forward in time*. This approach efficiently produces a detailed local size distribution without the necessity of integrating the trajectories of billions of droplets individually, which would have been the case if the usual strategy of following droplets which are uniformly distributed over the entire domain had been adopted.

Our numerical results demonstrate that the droplet size distribution becomes broader in the course of time due to turbulent dispersion of droplets both on large scales and on small scales. We show that it is essential to take this entire range of scales into account: Excluding the largest scales, for instance, does not result in a very broad spectrum of droplet sizes since all droplets in the simulation experience approximately the same supersaturation (a result found in Refs. 17,

18, and 22). Not taking into account the smallest scales does not show turbulent mixing of droplets of different sizes on the smallest scales,[20] an effect which is vital for the enhanced coalescence mechanism. Finally, it is demonstrated that although the effects of vapor depletion and the release of latent heat slow down the droplet growth, they do not qualitatively alter the broadening of the droplet size distribution at the smallest scales.

The present paper is organized as follows. In Sec. II the physical and mathematical models describing the turbulent velocity field and the condensation process are discussed. Two approaches are proposed for modeling the condensation process: a two-way coupled model in which the droplet growth has a feedback on the temperature and supersaturation fields, and a simplified model in which the feedback is neglected. The first part of Sec. III is devoted to the results for the statistics of droplet dispersion in the turbulent flow field. Subsequently, results are presented for the evolution of droplet size distributions, using either the simplified condensation model (Sec. III B) or the two-way coupled model (Sec. III C). Finally, the conclusions are formulated in Sec. IV.

II. PHYSICAL-MATHEMATICAL MODEL

The condensation of droplets in atmospheric clouds is a very complex process. It takes place if pre-existing CCNs are allowed to grow due to suitable values of vapor pressure and temperature. Condensing droplets release latent heat, thereby increasing the temperature of the surrounding mixture of dry air and water vapor. Simultaneously, the droplets are transported by a turbulent flow field over several hundreds of meters, which itself is affected by the condensation processes taking place on microscales. A further complication involves the expansion of a parcel of air as it rises, thereby inducing nonzero gradients in the density, pressure, and temperature fields of the mixture. Furthermore, many other phenomena take place in a cloud, such as additional temperature differences due to solar radiation (the higher parts of a cloud receive more light from the sun than the lower parts) and due to various chemical processes.[4,16,17]

Given this complex interaction between various processes, the development of a complete physical model, which takes into account all chemical, thermodynamic, and hydrodynamic phenomena occurring in actual atmospheric clouds, is an extremely challenging task. It is therefore not our intention to simulate an actual atmospheric cloud with all its intricate physics in this investigation. Instead, we aim to isolate and understand the influence of turbulence on the condensation process, for which the use of a simplified model is more appropriate.

In this regard, the main assumption that we make in the present research is that the velocity field of the air/vapor mixture in an atmospheric cloud corresponds to a statistically stationary homogeneous isotropic turbulent flow in three dimensions, independent of the presence of the condensing droplets. Of course, the presence of droplets is likely to influence the flow field, e.g., droplet evaporation may act as a source of kinetic energy due to cooling associated with the absorption of latent heat, coupled with buoyancy (see, e.g., Refs. 21 and 23). It is believed that such influences are primarily of importance at the edge of a cloud, where mixing with dry air takes place. Since our primary goal is to isolate the influence of turbulence on droplet condensation, we employ a simplified model which does not include feedback of the condensation process to the dynamics of the flow field. Therefore, we model the turbulent flow field by a kinematic simulation composed of random Fourier modes.[24] This approach has the major advantage that the flow model encompasses all turbulent length scales, from the integral scales to the Kolmogorov scales.

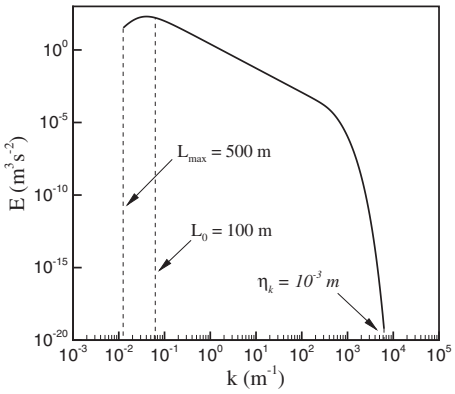

FIG. 1. Turbulent energy spectrum used in the kinematically simulated flow field. The integral length scale is $L_0=10^2$ m and the Kolmogorov length scale is $\eta_k=10^{-3}$ m.

A. Flow field composed of random Fourier modes

The flow of the air/vapor mixture is prescribed by a synthetic velocity field $\mathbf{u}(\mathbf{x},t)$ composed of N random Fourier modes,[24]

$$\mathbf{u}(\mathbf{x},t)=\sum_{n=1}^{N}[\mathbf{A}_n\cos(\mathbf{k}_n\cdot\mathbf{x}+\omega_n t)+\mathbf{B}_n\sin(\mathbf{k}_n\cdot\mathbf{x}+\omega_n t)], \quad (2)$$

where $\mathbf{A}_n$ and $\mathbf{B}_n$ are orthogonal to $\mathbf{k}_n$ so that an incompressible flow field is obtained which varies smoothly in both space and time. Determination of the random wave numbers $\mathbf{k}_n$, amplitude coefficients $\mathbf{A}_n$ and $\mathbf{B}_n$, and frequencies ω_n proceeds in similar fashion as described in Ref. 25 and is summarized in Appendix A. The prescribed turbulent energy spectrum is plotted in Fig. 1.

It is noted that the kinematic simulation (KS) of the velocity field in the present investigation does not take into account the sweeping of the smaller turbulent eddies by the larger ones, such as is the case in real turbulence (see, e.g., Ref. 26 and references therein). The absence of this sweeping mechanism may lead to quantitatively different Lagrangian droplet histories compared to actual atmospheric clouds, and thus the extent to which broadening of the droplet size distribution occurs may be significantly different. In qualitative sense, however, it is our belief that the present KS is still able to expose the basic role played by turbulence in the broadening of the droplet size distribution.

Using the KS-velocity field in Eq. (2), the droplets are advected by the turbulent flow like passive tracers. This is a

valid approximation in the present research since we focus primarily on droplets with sizes 10^{-7} m$<r_d<10^{-5}$ m, for which the Stokes number based on the Kolmogorov scales is $0.2\times10^{-5}<\mathrm{St}<0.02$, and the ratio between the settling velocity and the Kolmogorov velocity is $0.3\times10^{-4}<v_s/v_k<0.3$. Also, the Brownian motion is neglected since Brownian diffusion is much smaller than the turbulent diffusion for the flow fields that are simulated in this investigation. Thus, the position of a droplet in the course of time $\mathbf{x}_d(t)$ is given by

$$\frac{d\mathbf{x}_d}{dt}=\mathbf{u}[\mathbf{x}_d(t),t], \tag{3}$$

with $\mathbf{u}[\mathbf{x}_d(t),t]$ specified by Eq. (2).

B. Two-way coupled droplet condensation model

Let us consider one droplet of mass m_d, which moves in a turbulent velocity field $\mathbf{u}(\mathbf{x},t)$. The droplet is contained within an air/vapor parcel of volume V_c, which is assumed to be much larger than the droplet's volume, but small enough so that all molecules in the parcel remain together for a long time, i.e., the diffusive mass and energy transport at the outer surface of the parcel is neglected. Using this concept, we derive a model for the growth rate of the droplet. First, we introduce an expression for the supersaturation in the parcel based on a mass balance and, subsequently, we present the equation for the temperature following from an energy balance. We assume the temperature to remain uniform over the entire parcel, and that the vapor fully mixes instantaneously throughout the parcel.

The volume of the parcel V_c can be seen as the volume of air and vapor available per droplet. It is therefore related to the droplet number density n_d as

$$V_c=n_d^{-1}. \tag{4}$$

If the mass of air inside the parcel is denoted by m_a, the mass of vapor by m_v, and the mass of the droplet by m_d, a mass balance yields

$$\frac{d}{dt}(m_a+m_v+m_d)=0,\quad \frac{dm_v}{dt}=-\frac{dm_d}{dt}, \tag{5}$$

where we have used that only vapor can be transformed into liquid and vice versa.

Upon neglecting the droplet's volume, the partial vapor density ρ_v in the air/vapor mixture can be determined by

$$\rho_v=\frac{m_v}{V_c}, \tag{6}$$

and its time derivative along the droplet's trajectory is

$$\frac{d\rho_v}{dt}=\frac{1}{V_c}\frac{dm_v}{dt}-\frac{m_v}{V_c^2}\frac{dV_c}{dt}=-\frac{1}{V_c}\frac{dm_d}{dt}-\frac{m_v}{V_c^2}\frac{dV_c}{dt}. \tag{7}$$

The rate of change of V_c is not necessarily zero because the volume V_c may expand (shrink) when it is transported to higher (lower) altitudes. Since in atmospheric clouds $m_a\gg m_v+m_d$,[5] the evolution of V_c in time can, in principle, be determined from $V_c=m_a/\rho_a$, where ρ_a denotes the partial density of air. It can be shown that the variation of ρ_a is so weak in atmospheric clouds that the influence of the second term on the right-hand side of Eq. (7) is negligible compared to the other thermodynamical effects. Thus, we take

$$\frac{dV_c}{dt}=0 \tag{8}$$

and, as a consequence of Eq. (4), n_d can be considered constant as well.

The law describing the condensational growth of a droplet varies considerably with the droplet's size. For very small droplets (i.e., large Knudsen number) the growth is described by the Hertz–Knudsen law which includes the so-called Kelvin effect,[4] whereas the growth rate of large droplets (i.e., for small Knudsen number) is governed by diffusion. For the sake of simplicity, we employ the diffusional growth law for all droplet sizes in the present study, which is similar to the approach by Twomey,[15] Celani *et al.*,[20] and Lanotte *et al.*[21] Although this growth law overestimates the droplet growth rate for the smallest droplets of size $r_d\lesssim10^{-7}$ m, it is accurate for the majority of the droplets in our simulations whose radius is generally much larger than the capillary length scale. The diffusional growth law for a stagnant spherical droplet in a quiescent vapor is[27]

$$\frac{dm_d}{dt}=4\pi r_d^2\rho_d\frac{dr_d}{dt}=\dot{m}_d=4\pi r_d D_{\mathrm{va}}(\rho_v-\rho_v^s), \tag{9}$$

where D_{va} is the binary diffusion coefficient of water vapor in air, ρ_d is the bulk density of water ($\rho_d=10^3$ kg/m^3), and ρ_v^s denotes the saturation vapor density, which depends on the temperature: $\rho_v^s=\rho_v^s(T)$ (see Appendix B).

Strictly speaking, Eq. (9) is valid for an isolated droplet which moves like a passive tracer in a uniform flow field. Such conditions are generally not satisfied for a dispersion of condensing droplets carried within a turbulent flow field. In atmospheric clouds, however, the interdroplet separation distance d_s is typically much larger than the droplet radius during the condensation stage, $d_s\sim10^{-3}$ m$\gg r_d\sim10^{-5}$ m, which means that the condensation process indeed takes place as if the droplets were isolated from each other. With respect to the influence of turbulence, it is noted that due to the velocity gradients in such flow fields, the growth law in Eq. (9) needs to be modified to account for the presence of a convective wind which contributes to the transfer of vapor toward the surface of the droplet.[28] The importance of this convective transport compared to the diffusive transport is quantified by means of the Peclet number Pe,

$$\mathrm{Pe}\equiv\frac{u_c r_d}{D_{\mathrm{va}}}, \tag{10}$$

in which u_c is the convective velocity of the vapor. Since the droplet radius is much smaller than the Kolmogorov length scale ($r_d^{\max}\sim10^{-5}$ m$\ll\eta_k=10^{-3}$ m), the local velocity gradients at the length scale of the droplet are $\sim\tau_k^{-1}$, which results in a convective velocity of $u_c\sim r_d/\tau_k$. With $D_{\mathrm{va}}\sim10^{-5}$ m^2/s under atmospheric conditions, and using a value of $\tau_k\sim10^{-2}$ s as typically reported for the Kolmogorov time scale in atmospheric clouds, the resulting Peclet

number becomes $\mathrm{Pe} \sim 10^{-3} \ll 1$. Thus, the convective contribution in the mass transfer of vapor can be neglected compared to the diffusive transport. Considering the above arguments, it is concluded that Eq. (9) is a valid approximation for the condensation process in the present investigation.

By introducing the supersaturation s of the moist air surrounding the droplet,

$$s \equiv \frac{\rho_v}{\rho_v^s} - 1, \tag{11}$$

we can rewrite Eq. (9) as

$$\dot{m}_d = 4\pi r_d D_{\mathrm{va}} s \rho_v^s. \tag{12}$$

The rate of change of the supersaturation can be obtained by differentiating Eq. (11) with respect to time and making use of Eqs. (7), (8), and (12) in order to obtain

$$\frac{ds}{dt} = -\frac{s}{\tau_s} - (s+1)\frac{dT}{dt}\frac{d}{dT}(\ln \rho_v^s), \tag{13}$$

where the vapor depletion time scale τ_s is given by

$$\tau_s = \frac{V_c}{4\pi r_d D_{\mathrm{va}}} = \frac{1}{4\pi r_d D_{\mathrm{va}} n_d}. \tag{14}$$

An equation for the temperature of the moist air surrounding the droplet can be obtained by considering the conservation of energy in the volume V_c. For a system of this size, the variation of the enthalpy within the volume V_c is negligible, and therefore the conservation of energy is given by

$$\frac{d}{dt}(m_a h_a + m_v h_v + m_d h_d) = -(m_a + m_v + m_d)\mathbf{u} \cdot \mathbf{e}_z g, \tag{15}$$

where h_a, h_v, and h_d denote the specific enthalpy of the air, vapor, and droplet, respectively. Equation (15) expresses the balance between the change in the energy of the parcel and the work done by gravity, as viscous dissipation and thermal heat conduction are neglected. Since the supersaturation is close to zero,[5] the liquid enthalpy h_d may be approximated by

$$h_d = h_v - \mathcal{L}, \tag{16}$$

where $\mathcal{L} = \mathcal{L}(T)$ is the latent heat of vaporization. By employing a caloric equation of state $h_a = C_{p,a}T$ and $h_v = C_{p,v}T$ (with $C_{p,i}$ denoting the isobaric specific heat of substance i, see Appendix B), in combination with Eqs. (5) and (16), Eq. (15) may be cast into the following form:

$$\frac{dT}{dt} = \frac{\dot{m}_d \mathcal{L} - (m_a + m_v + m_d)\mathbf{u} \cdot \mathbf{e}_z g}{m_a C_{p,a} + (m_v + m_d)C_{p,v} - m_d d\mathcal{L}/dT}. \tag{17}$$

Since in atmospheric clouds it holds that $m_a C_{p,a} \gg (m_v + m_d)C_{p,v}$ and $m_a C_{p,a} \gg m_d d\mathcal{L}/dT$, Eq. (17) may be further simplified to

$$\frac{dT}{dt} = \frac{\dot{m}_d \mathcal{L} n_d}{\rho_a C_{p,a}} - \Gamma \mathbf{u} \cdot \mathbf{e}_z, \tag{18}$$

where the factor Γ is the so-called adiabatic lapse rate,[5] given by

$$\Gamma = \frac{g}{C_{p,a}}. \tag{19}$$

The two-way coupled system is now closed and it can be solved along the trajectory of a droplet in the course of time. Specifically we need to solve Eqs. (13) and (18) for the supersaturation and temperature of the moist air surrounding the droplet, respectively, and Eq. (12) for the rate of change of the droplet mass, using some initial conditions for $s(t=0)$, $T(t=0)$, and $m_d(t=0)$. This system of ordinary differential equations is augmented by Eq. (14) for the saturation relaxation time τ_s, as well as the expressions for the quantities $D_{\mathrm{va}}(p,T)$, $\mathcal{L}(T)$, and $\rho_v^s(T)$ and the material constant $C_{p,a}$, which are all given in Appendix B. Finally, the parameters ρ_a and n_d can be chosen freely depending on the problem at hand.

We refer to this model as the "two-way coupled condensation model." It should be noted that Eq. (13) is actually very similar to the expression used by Twomey to calculate the variation in the supersaturation in Ref. 15. Although the effect of latent heat release had been excluded in that particular investigation, recent works by Celani *et al.*[20] and Lanotte *et al.*[21] do take it into account by means of an appropriate sink term in the balance equation for the supersaturation. The main difference between our two-way coupled condensation model and those of Refs. 20 and 21 is that the latter use an Eulerian formulation to describe the evolution in s, whereas we employ a Lagrangian approach.

C. Simplified droplet condensation model

As can be noted from Eqs. (13) and (18), the supersaturation changes due to three effects: adiabatic cooling, vapor depletion (i.e., the finiteness of V_c), and the release of latent heat by the condensing droplet. The latent heat release and the vapor depletion term tend to slow down the growth of droplets and thus have a stabilizing effect on the development of the droplet size distribution in r_d-space. Adiabatic cooling, however, is the only mechanism capable of increasing the supersaturation when a droplet is growing. It can therefore be seen as the only stimulating effect on the condensation process. Indeed, adiabatic cooling is widely believed to be the main source of supersaturation, and therefore of the condensational growth of droplets in a cloud.[1,19]

In order to isolate the effect of adiabatic cooling, we propose a simplified condensation model in which the effects of vapor depletion and latent heat release are neglected. This approach has two advantages: First, it allows us to determine the influence of adiabatic cooling on the development of the droplet size distribution, without the results being obscured by secondary effects. Second, in a subsequent stage, the results obtained with the simplified condensation model can be compared to the results from the two-way coupled condensation model. Any differences between the results can unambiguously be related to the feedback of the droplet growth on the temperature and supersaturation fields.

The simplified condensation model follows readily from the two-way coupled condensation model presented in Sec. II B. If latent heat release is neglected, Eq. (18) reduces to

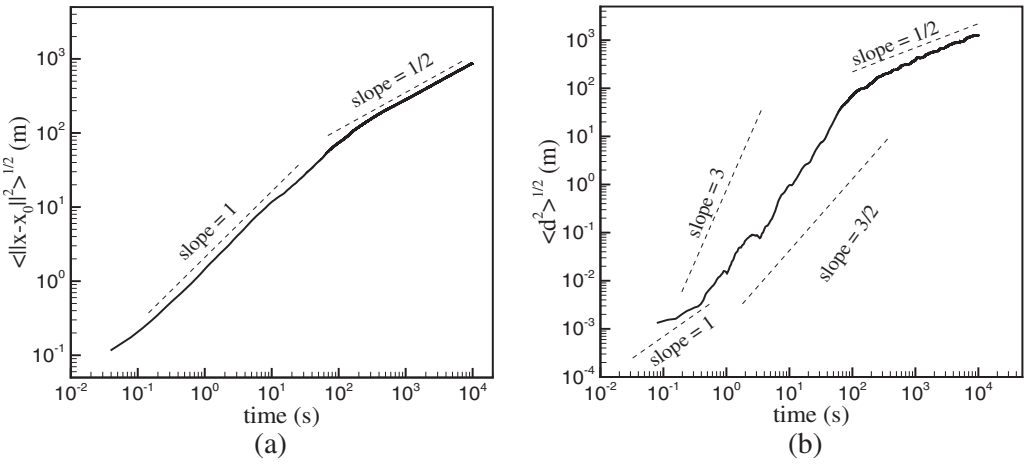

FIG. 2. (a) Lagrangian one-particle statistics, based on simulation data obtained for 500 droplets in five different realizations of the flow field composed of 200 random Fourier modes; (b) Lagrangian two-particle statistics, based on simulation data obtained for 500 droplet pairs in five different realizations of the flow field composed of 200 random Fourier modes. The initial interparticle separation distance is equal to the Kolmogorov length scale: $d_0=\eta_K=10^{-3}$ m.

$$\frac{dT}{dt}=-\Gamma\mathbf{u}\cdot\mathbf{e}_z. \tag{20}$$

Similarly, if the effect of vapor depletion is neglected, all terms involving the finiteness of the volume V_c are zero and Eq. (13) becomes

$$\frac{ds}{dt}=-(s+1)\frac{dT}{dt}\frac{d}{dT}(\ln\rho_v^s)=(s+1)\Gamma\mathbf{u}\cdot\mathbf{e}_z\frac{d}{dT}(\ln\rho_v^s). \tag{21}$$

Finally, the droplet growth law is still given by Eq. (9).

We refer to this model, which is similar to the model employed by Celani *et al.*[19] as the "simplified condensation model," which accounts for condensation in a prescribed temperature field resulting from adiabatic expansion cooling.

III. RESULTS

A. Statistics of droplet dispersion

Before presenting the results for the condensation models, we briefly discuss some statistics of the one- and two-droplet dispersions in the turbulent flow described by Eq. (2), with the coefficients given in Appendix A. Here and in the following, we choose the integral length scale of the flow as $L_0=10^2$ m and the Kolmogorov length scale as $\eta_k=10^{-3}$ m.

In this flow field, the trajectories of droplets in the course of time are determined by integrating Eq. (3) numerically using a fourth-order Runge–Kutta scheme. The numerical time step in all simulations presented here is fixed at $\Delta t=0.1/\omega_N$ so that the motion of a droplet through the smallest turbulent eddies is resolved with sufficient accuracy. Convergence tests have been done with smaller values of Δt, and the results for the dispersion or the condensation of droplets were not significantly different.

First, we investigate the one-droplet dispersion by calculating the trajectories of 500 droplets in five different realizations of the flow field. Each droplet is released at a random point $\mathbf{x}_d(0)$ and traced for a time $0\le t\le 10^4$ s, during which the distance to the point of injection $\|\mathbf{x}_d(t)-\mathbf{x}_d(0)\|$ is calculated. The square root of the squared distance averaged over all droplets $\langle\|\mathbf{x}_d(t)-\mathbf{x}_d(0)\|^2\rangle^{1/2}$ is plotted in Fig. 2(a) as a function of time. The result shows that the droplets in an atmospheric cloud can be transported over distances of the order of 100 m within a time span of 100 s. In addition, it is clear that $\langle\|\mathbf{x}_d(t)-\mathbf{x}_d(0)\|^2\rangle^{1/2}\propto t$ for small values of t, and $\langle\|\mathbf{x}_d(t)-\mathbf{x}_d(0)\|^2\rangle^{1/2}\propto t^{1/2}$ for large values of t, which is perfectly in agreement with Taylor's famous prediction of one-particle dispersion in a turbulent flow.[29]

The statistics of the two-droplet dispersion are determined by releasing 500 pairs of droplets at an initial separation d_0 in five different realizations of the flow. The initial distance is chosen as $d_0=\eta_k$ and the direction of the interparticle separation vector is selected randomly in three dimensions. The trajectory of each droplet in a droplet pair is calculated from Eq. (3), and at each time step the distance between the droplets $d(t)$ is measured. Averaging over all droplet pairs then results in $\langle d^2(t)\rangle^{1/2}$, which is plotted in Fig. 2(b) as a function of time. The separation distance is apparently proportional to t for small values of t, and proportional to $t^{1/2}$ for very large values of t. In the intermediate time range, the separation distance in a turbulent flow should be proportional to $t^{3/2}$ when the separation distance is of the order of the size of the eddies in the turbulent inertial range, as the classic theory by Richardson[30] predicts. Based on our limited statistics we are not sure whether or not our kinematic simulation produces exactly that behavior, but we do see a range in which $\langle d^2(t)\rangle^{1/2}\propto t^p$, with p somewhere between $3/2<p<3$. This result is generally in agreement with recent literature, such as Thomson and Devenish[31] who claimed $p=2.3$, and Osborne *et al.*[26] who showed that p may vary with different choices of the unsteadiness parameter λ [see Eq. (A7)].

Regardless of whether or not the current kinematic simulation exactly produces Richardson's law, it is clear from Fig. 2(b) that two droplets which are initially separated by a small distance may end up in completely different regions of the flow after a sufficiently long time. Vice versa, since the equation of motion Eq. (3) is reversible in time, it also holds that two droplets which are nucleated at two distantly separated positions, may end up very close to one another at some

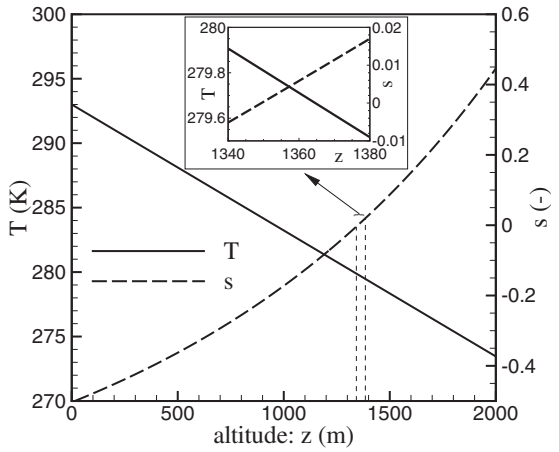

FIG. 3. Temperature and supersaturation profiles as a function of altitude z. At the earth's surface $z=0$, $T=293$ K, and $s=-0.5$. Inset: close-up of region where $s \simeq 0$.

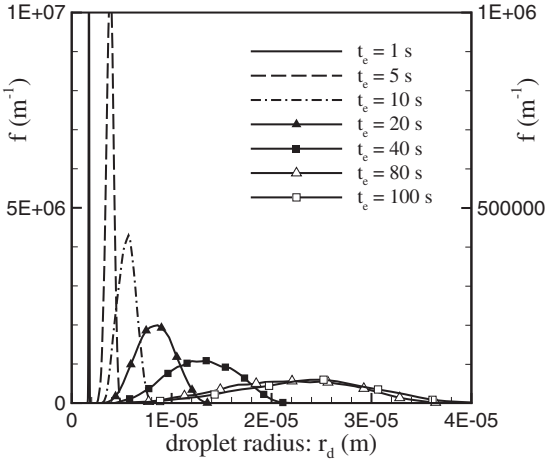

FIG. 4. Droplet radius distribution function $f(r_d)$ for seven different moments in time t_e. The final altitude of droplets $z_e=1350$ m and the sampling area $L^2=(500\ \text{m})^2$. The results have been obtained with the simplified condensation model.

instant of time. This concept turns out to be essential for the explanation of the results obtained with the condensation models.

B. Results for simplified condensation model

In the present section we discuss the results obtained for the simplified condensation model. The size of a droplet at a final time t_e is obtained in two steps: First we calculate the trajectory of the droplet backward in time (i.e., from $t=t_e$ to $t=0$), and subsequently, we determine the droplet growth rate forward in time along this trajectory. In the first step, the position of the droplet follows from

$$\frac{d\mathbf{x}_d}{d\tau} = -\mathbf{u}[\mathbf{x}_d(\tau),\tau], \quad \mathbf{x}_d(\tau=0)=\mathbf{x}_d(t=t_e)=\mathbf{x}_{d,e}, \tag{22}$$

with $\tau=t_e-t$ running from 0 to t_e, and $\mathbf{u}[\mathbf{x}_d(\tau),\tau]$ prescribed by Eq. (2). The final position $\mathbf{x}_{d,e}=(x_e,y_e,z_e)^T$ is specified by choosing an altitude z_e, whereas the horizontal coordinate (x_e,y_e) is chosen randomly in a square with sides of length L. In each simulation, $N_{d,\text{tot}}=16\,000$ droplets are traced backward in time starting from these final positions. This procedure efficiently produces droplet size statistics within the sampling areas $x\in[0,L]$, $y\in[0,L]$, and $z=z_e$ at time $t=t_e$, while it avoids the necessity to follow a huge number of particles uniformly distributed over the entire domain, like in traditional Eulerian–Lagrangian methods.

Once the trajectory of a droplet is known, Eq. (9) for the droplet mass $m_d(t)$ is solved forward in time, starting from the initial condition $m_d(0)$. All droplets are supposed to have the same size $r_0=10^{-7}$ m initially so that $m_d(0)=(4\pi/3)\rho_d r_0^3$. It is noted that for the simplified model, the local temperature and supersaturation values are obtained from a prescribed profile (see Fig. 3), for which the data are obtained from the adiabatic cooling of a parcel of rising air. The profiles $T(z)$ and $s(z)$ are given by

$$T(z)=T(z=0)-\Gamma z \quad \text{and} \quad s(z)=\frac{\rho_v}{\rho_v^s[T(z)]}-1, \tag{23}$$

where the vapor density ρ_v is supposed be constant because its variations are much smaller than the variations in ρ_v^s. The vapor density is therefore set equal to its value at the earth's surface. For all the simulations presented in this paper, the conditions at the earth's surface ($z=0$) are taken as $T(z=0)=20\ ^\circ\text{C}=293$ K, with a relative humidity of 50% ($s=-0.5$).

Given Eq. (9), it is obvious that a droplet may shrink to a mass of zero, if it experiences negative supersaturation for a sufficiently long time. Physically, this means that it is completely evaporated. If such happens, the droplet is eliminated from the calculation and makes no contribution to the size distribution function.

In Fig. 4 we show the droplet size distribution for $z_e=1350$ m and a sampling area $L^2=(500\ \text{m})^2$, for seven different values of t_e. The distribution function is a Dirac delta function at $t_e=0$ and becomes broader for larger t_e. Already after $t_e=20$ s, some droplets have reached a size of tens of microns, which is remarkable because the supersaturation at $z_e=1350$ m is very close to zero (see Fig. 3). The explanation of the spectral broadening lies in turbulent dispersion:[19] Droplets with different histories are located in the sampling space situated at altitude z_e at time t_e. Droplets which have been at higher altitudes have experienced higher supersaturations and thus have grown more than droplets which have been at lower altitudes. The ongoing broadening of the size distribution depicted in Fig. 4 shows that the theory by Twomey[15] is fundamentally wrong because it does not account for turbulent dispersion.

In Fig. 5 we compare the droplet size distributions after time $t_e=100$ s at five different altitudes z_e. Sampling spaces at high altitudes z_e are predominantly populated by droplets which (on average) have experienced higher supersaturations than droplets at low altitudes (see Fig. 3). Therefore, the mean size of droplets at high z_e is larger than at low z_e, and this trend is clearly visible in Fig. 5. The variance of $f(r_d)$,

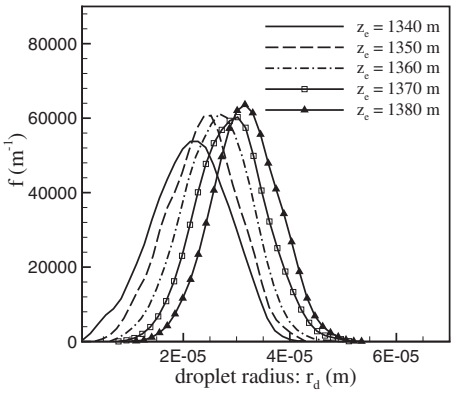

FIG. 5. Droplet radius distribution function $f(r_d)$ for five different final altitudes of droplets z_e. The sampling time $t_e=100$ s and the sampling area $L^2=(500\ \mathrm{m})^2$. The results have been obtained with the simplified condensation model.

however, does not seem to be affected much by the altitude, as the droplet size distributions are relatively broad for all altitudes considered.

We determine the fraction of evaporated droplets by counting the number of evaporated droplets $N_{d,\mathrm{evap}}$ in the simulations presented in Fig. 5 and comparing them to the total number of droplets $N_{d,\mathrm{tot}}$ initially released in the flow. The ratio $N_{d,\mathrm{evap}}/N_{d,\mathrm{tot}}$ is plotted in Fig. 6. It is clear that more droplets evaporate at lower values of z_e, which is a consequence of the supersaturation being smaller at lower altitudes, and therefore, the fraction of droplets experiencing negative supersaturation is higher. The high initial evaporation rate is due to the fact that some of the droplet trajectories have a starting point $z_d(0)$ in a region where $s<0$: These droplets evaporate almost immediately.

It is important to note that droplet nucleation after $t=0$ is not taken into account in our model. In reality, however, a new droplet may grow along the trajectory of a previously evaporated droplet. We neglect the regeneration of droplets for the sake of simplicity, but this phenomenon is likely to be present in atmospheric clouds and could eventually result in a multimodal droplet size distribution function.

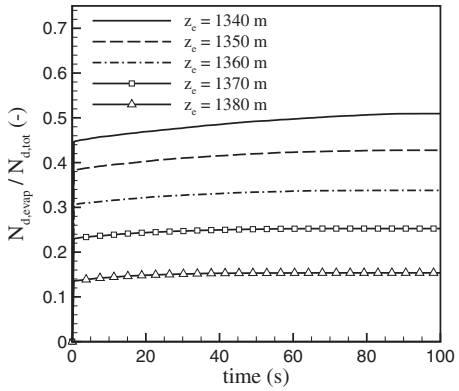

FIG. 6. Number of evaporated droplets relative to the total number of droplets in the simulation as a function of time, for five different final altitudes z_e after time $t_e=100$ s. The results have been obtained with the simplified condensation model with $L^2=(500\ \mathrm{m})^2$.

We now give a brief interpretation of the results in terms of the relevant parameters of the problem which ultimately determine the temperature and supersaturation profiles. By doing so, we provide an analytical estimate for the broadening of the droplet size distribution function in the course of time. It follows from Eq. (9) that the surface of the droplet $\Sigma_d(t)\equiv 4\pi r_d^2(t)$ changes as

$$\dot{\Sigma}_d = Gs, \quad \text{with } \Sigma_d(0)=4\pi r_0^2, \tag{24}$$

where $G=8\pi D_{\mathrm{va}}\rho_v^s/\rho_d$. Most droplets in our simulations experience temperature variations that are so small that G remains approximately constant. In addition, in the simplified condensation model, the equation for the supersaturation, Eq. (13), can be integrated to obtain

$$s(t)=s[z_d(t)]=A[z_d(t)-z_{\mathrm{ref}}] \tag{25}$$

for a constant value of the parameter $A=\Gamma d(\ln \rho_v^s)/dT$, which is a reasonable approximation in our case where the temperature variations are relatively weak. In fact, Eq. (25) stems from a local linearization of the adiabatic supersaturation profile shown in Fig. 3. The value z_{ref} denotes the reference altitude for which the supersaturation is zero. It is easy to integrate Eq. (24) along the trajectory of a droplet using Eq. (25), and the result is

$$\Sigma_d(t)=4\pi r_0^2+GA\zeta(t) \tag{26}$$

with

$$\zeta(t)\equiv\int_0^t [z_d(t')-z_{\mathrm{ref}}]dt'. \tag{27}$$

Thus, $\Sigma_d(t)$ is proportional to $\zeta(t)$ and their statistics, determined by averaging over a large number of droplets, are similar,

$$\mathrm{PDF}(\zeta)=\mathrm{PDF}\left(\frac{\Sigma_d-4\pi r_0^2}{GA}\right), \tag{28}$$

where PDF denotes the probability distribution function. In other words, one could, in principle, estimate the droplet size distribution at a given altitude z_e by using only the statistics for the dispersion.

We show the PDF of ζ at $t_e=100$ s in Fig. 7 for droplets which have a final position in a sampling area of size $L^2=(500\ \mathrm{m})^2$ at altitude $z_e=1350$ m. In the same graph, we also show the PDF of the mean supersaturation $s_m(t_e)$ along the trajectory of a droplet, defined as

$$s_m(t)\equiv\frac{1}{t}\int_0^t s(t')dt. \tag{29}$$

It is noted that we include *all* droplet trajectories in generating these PDFs, i.e., including those for which droplets evaporate completely. In order to allow direct comparison, the PDFs are shown as a function of the scaled standardized variables,

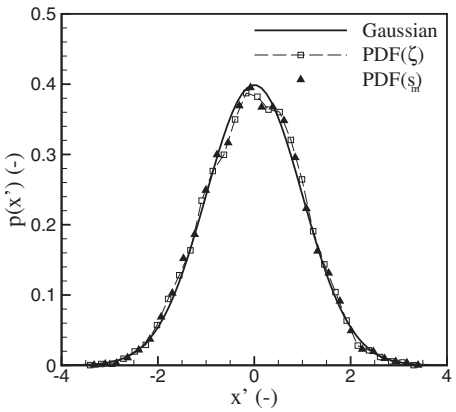

FIG. 7. Standardized PDFs of ζ [see Eq. (27)] in the simulation (based on data for all droplets, i.e. evaporated or not) and the mean supersaturation s_m along their trajectories. For the sake of comparison, a Gaussian distribution with zero mean and unity variance is plotted as well. The sampling time $t_e=100$ s, the final altitude of droplets $z_e=1350$ m, and the sampling area $L^2=(500\ \mathrm{m})^2$. The results have been obtained with the simplified condensation model.

$$x'_\zeta \equiv \frac{\zeta - \langle\zeta\rangle}{\sqrt{\mathrm{var}(\zeta)}}, \quad x'_{s_m} \equiv \frac{s_m - \langle s_m\rangle}{\sqrt{\mathrm{var}(s_m)}}, \tag{30}$$

where $\mathrm{var}(\cdot)$ stands for the variance obtained from averaging over all droplets. We see a perfect agreement, as is expected from the linearity of Eq. (25). In addition, it is noteworthy that the PDFs are symmetric, which follows from the isotropy of the flow field, and furthermore, they are almost perfectly Gaussian.

Next, we investigate the correlation between the parameter ζ and Σ_d. In Figs. 8(a) and 8(b) we show the PDF of the normalized quantities x'_ζ and x'_{Σ_d} (with x'_{Σ_d} obtained analogously to x'_ζ) only for droplets that have *not* evaporated, for sampling altitudes $z_e=1350$ m and $z_e=1380$ m, respectively. In both figures we see a perfect agreement between x'_ζ and x'_{Σ_d}, which confirms our analysis presented in Eq. (28). From comparing Fig. 8(a) with Fig. 8(b), it is clear that the PDF of x'_{Σ_d} is more symmetric for higher z_e. This can be explained as follows. Any asymmetry in the graphs is purely due to the evaporation of droplets because the PDF of ζ measured for all droplets (evaporated and nonevaporated) should be symmetric due to the isotropy of the turbulent flow. If z_e increases, the number of evaporated droplets decreases (see Fig. 6) and therefore, the standardized PDF of Σ_d becomes more symmetric. Figures 8(a) and 8(b) also show the PDF of the standardized droplet radius x'_{r_d}, which is remarkably close to Gaussian. This is probably a coincidence since there is no evidence that the PDF of r_d is directly governed by a Gaussian process.

The evolution of the mean and variance of the PDF of Σ_d in the course of time can be estimated on the basis of the mean and the variance of the PDF of ζ. Since

$$z_d(t) = z_e - \int_t^{t_e} w(t')dt', \tag{31}$$

where w is the vertical velocity component of the flow field, and due to symmetry, it is clear that $\langle\zeta\rangle=(z_e-z_{\mathrm{ref}})t$. The variance $\langle\zeta^2\rangle-\langle\zeta\rangle^2$ is given by

$$\langle\zeta^2\rangle - \langle\zeta\rangle^2 = 2\langle w^2\rangle \int_0^t \int_0^{t'} \xi(t',t'';t_e)dt''dt', \tag{32}$$

where

$$\xi(t',t'';t_e) = \int_{t'}^{t_e}\int_{t''}^{t_e} R(|\alpha-\beta|)d\alpha d\beta. \tag{33}$$

Here, $R(|x|)$ is the Lagrangian correlation coefficient for which $R(0)=1$, and

$$\int_0^\infty R(x)dx = \tau_w, \tag{34}$$

where τ_w denotes the integral time scale. Due to statistical stationarity of the flow field, the term $\langle w^2\rangle$ is a constant. Differentiation of Eq. (32) then yields

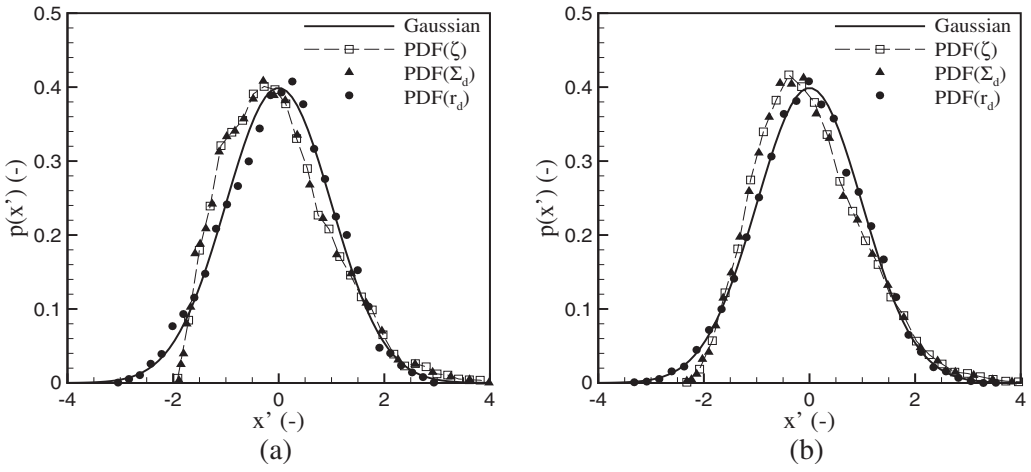

FIG. 8. Standardized PDFs of ζ [see Eq. (27)], the droplet radius r_d, and the droplet surface area Σ_d for *nonevaporated* droplets. For the sake of comparison, a Gaussian distribution with zero mean and unity variance is plotted as well. The results have been obtained with the simplified condensation model for sampling time $t_e=100$ s and the sampling area $L^2=(500\ \mathrm{m})^2$. (a) The final altitude of droplets $z_e=1350$ m. (b) The final altitude of droplets $z_e=1380$ m.

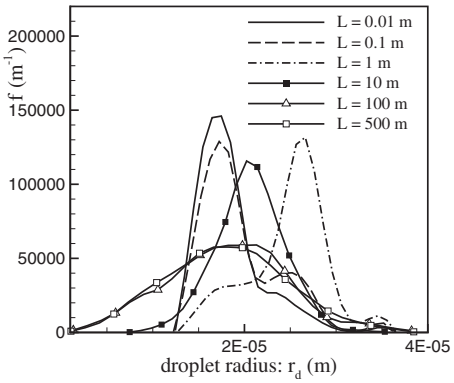

FIG. 9. Droplet radius distribution function $f(r_d)$ as a function of the droplet radius r_d, for six different sampling areas L^2 in one realization of the flow field. The sampling time $t_e=100$ s and the final altitude of droplets $z_e=1350$ m. The results have been obtained with the simplified condensation model.

$$\frac{d}{dt}(\langle\zeta^2\rangle-\langle\zeta\rangle^2)=2\langle w^2\rangle\int_0^t \xi(t,t';t_e)dt'. \tag{35}$$

As $R(x)>0$, it follows also that $\xi(t,t';t_e)>0$ and, therefore, we find $d/dt(\langle\zeta^2\rangle-\langle\zeta\rangle^2)>0$, implying that for an ensemble of droplets, the variance in $\zeta(t)$ increases as we follow the droplets in the course of time. We can estimate the mean and the variance of the droplet surface distribution PDF(Σ_d) at altitude z_e in the course of time as

$$\begin{aligned}\langle\Sigma_d\rangle &= 4\pi r_0^2+GA\langle\zeta\rangle(t)=4\pi r_0^2+GA(z_e-z_{\mathrm{ref}})t,\\ \frac{d}{dt}(\mathrm{var}(\Sigma_d)) &= 2G^2A^2\langle w^2\rangle\int_0^t \xi(t,t';t_e)dt'.\end{aligned} \tag{36}$$

This shows that the average droplet size increases when $z_e>z_{\mathrm{ref}}$, and that the PDF of Σ_d becomes broader in the course of time. Note that this analysis is only valid if droplet evaporation can be neglected.

Finally, we investigate whether a broad size distribution is observed in small sampling spaces. We calculate the droplet distribution in sampling areas of six different sizes L^2 in one realization of the flow field and show the result in Fig. 9. It appears that the droplet size distribution is broad in all sampling areas, also within sampling areas of the size of $L^2=(1\ \mathrm{cm})^2$. It is thus demonstrated that the condensation process leads to a broad size distribution within volumes comparable to the smallest scales of turbulence. Like the explanation of Celani *et al.*,[19] both large scales and small scales are responsible for the spectral broadening at small scales: Large scales are necessary to create sufficiently large differences in supersaturation among droplets, whereas the small-scale fluctuations can mix droplets of different sizes. This process can be illustrated in our model by calculating the droplet size distribution in a small sampling area of size $L^2=(1\ \mathrm{cm})^2$ in a flow field in which only the large-scale wavemodes $1\le n\le 10$ are accounted for in Eq. (2), and in a simulation in which only the small-scale wavemodes $191\le n\le 200$ are considered. In Fig. 10(a) we compare both results with the predictions for $L^2=(1\ cm)^2$ in which all 200 wavemodes have been taken into account. Apparently, neither the model in which the small scales have been neglected, nor the simulation in which the large scales have been neglected are able to predict a broad size distribution in a small sampling space. Furthermore, Fig. 10(b) shows that the distribution is nearly uniform in case only the large scales of motion are included, whereas the distribution tends to be Gaussian-like when only the smallest scales are considered. Since both size distributions are very narrow, it is clear that a realistic model for droplet condensation in clouds should include both the large scales and the small scales of turbulence, as both of them are vital in the process of spectral broadening.

All results in this section have been obtained with the simplified condensation model, which does not take into ac-

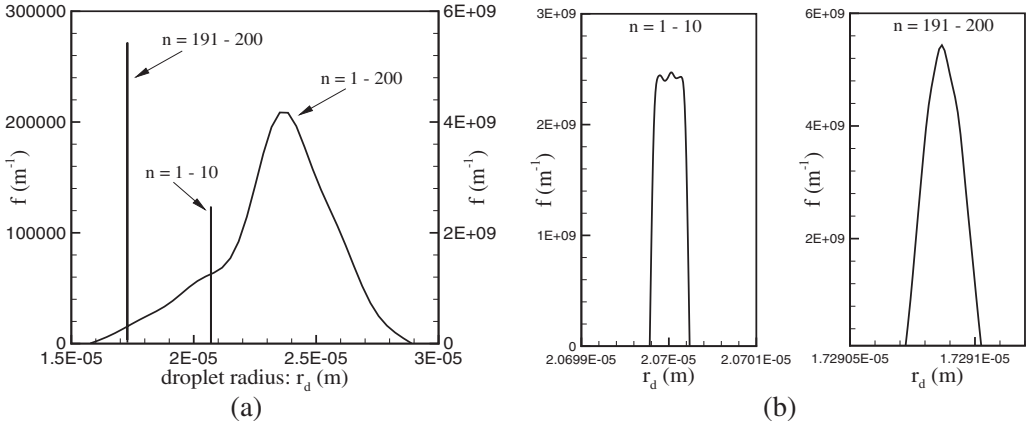

FIG. 10. Droplet radius distribution function $f(r_d)$ for three different flow fields: one with only the largest scales taken into account ($1\le n\le 10$, correspondingly: $1.26\times10^{-2}\le k\le 2.74\times10^{-2}$ m^{-1}), one with only the smallest scales taken into account ($191\le n\le 200$, correspondingly: $3.47\times10^{3}\le k\le 6.28\times10^{3}$ m^{-1}), and one with all scales taken into account ($1\le n\le 200$). (a) shows all three results in one figure, where the droplet size distribution function obtained with the full spectrum ($1\le n\le 200$) should be read from the left vertical scale and the other two from the right vertical scale; (b) shows close-ups of the droplet size distribution function for the large and small scales. The sampling time $t_e=100$ s, the final altitude of droplets $z_e=1350$ m, and the sampling area $L^2=(0.01\ \mathrm{m})^2$. The results have been obtained with the simplified condensation model.

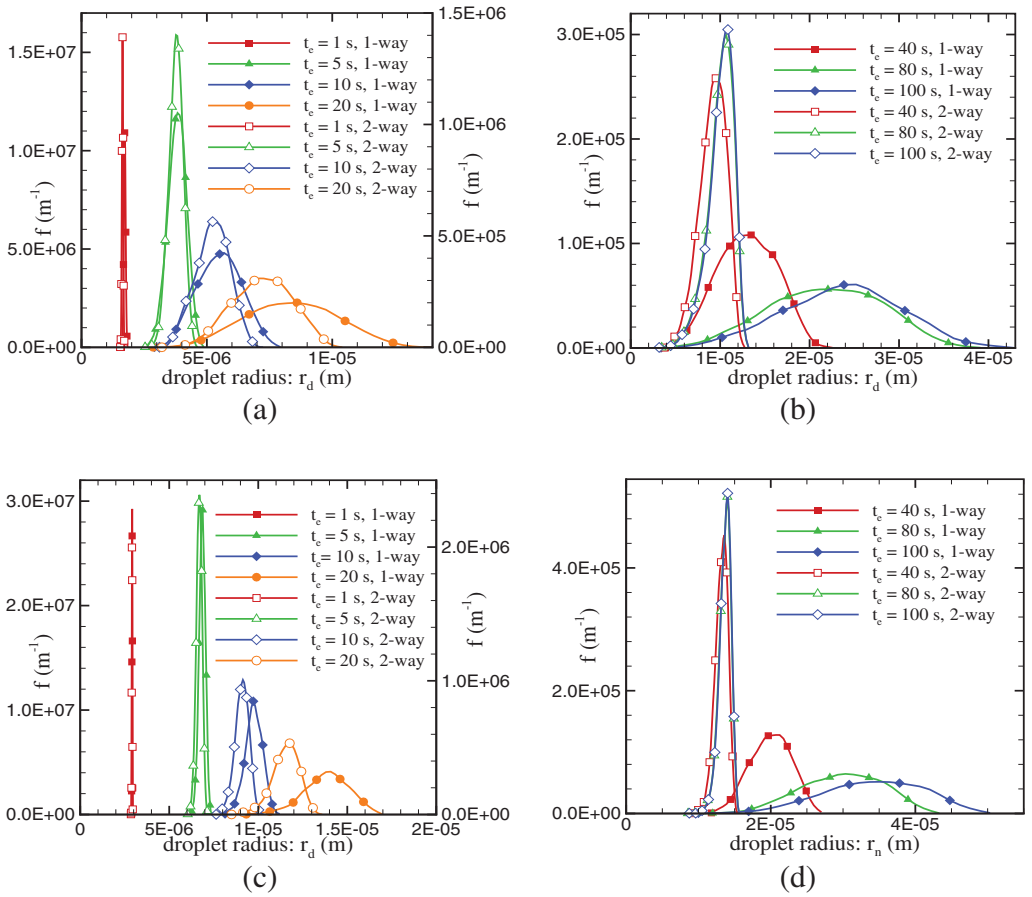

FIG. 11. (Color online) Droplet radius distribution function $f(r_d)$ for seven different instants of time t_e: (a) and (b) correspond to z_e=1350 m, (c) and (d) correspond to z_e=1380 m. In (a) and (c), the size distributions for $t_e \geq 5$ s are plotted on the right vertical scale. The lines with open symbols have been obtained with the two-way coupled condensation model, with $L^2=(500\ \text{m})^2$ and $N_l=(5\eta_k)^{-3}=0.8\times10^7\ \text{m}^{-3}$. The data for the one-way coupled simulation obtained with the same parameter settings (filled symbols, also see Fig. 4) are shown for comparison.

count the feedback of the droplet condensation on the carrier flow. The extent to which these phenomena affect the growth of droplets is quantified in Sec. III C.

C. Results for two-way coupled condensation model

We now present the results for the two-way coupled condensation model. The initial conditions for the droplet radius, temperature, and supersaturation are the same as in the simplified condensation model, and the same holds for the numerical methods used. In the two-way coupled model, two additional parameters have to be chosen in comparison to the simplified model: the partial air density, which has only minor variations in clouds, is assigned a constant value of ρ_a=1.2 kg m^{-3} in all simulations, whereas the droplet number density n_d, which may differ from cloud to cloud, is systematically varied in the following.

First, the evolution of the droplet size distribution is shown in Figs. 11(a) and 11(b) for an altitude of z_e=1350 m, and in Figs. 11(c) and 11(d) for an altitude of z_e=1380 m. The sampling area is taken as $L^2=(500\ \text{m})^2$, whereas the droplet number density is chosen as $N_l=(5\eta_k)^{-3}$. The data obtained with the simplified coupled model (using the same parameter settings) are also shown (indicated by the lines with filled symbols, also see Fig. 4) for comparison. From these figures it is clearly observed that vapor depletion and latent heat slow down the droplet growth considerably so that the mean droplet size predicted with the two-way coupled model is consistently smaller than that predicted with the simplified coupled model. The differences between the two models are especially manifest for $t_e > 10$ s, as the variance of the droplet size distribution for the two-way coupled model is significantly smaller. The initial growth of droplets from sizes of 0.1–5 μm does not seem to be significantly affected by vapor depletion and latent heat.

The results plotted in Figs. 11(c) and 11(d) for the higher altitude z_e=1380 m show the same trends as those corresponding with z_e=1350 m. For both altitudes, the droplet size distributions tend to a steady state, as the results corresponding to t_e=80 s and t_e=100 s are almost identical. As can be expected from the analysis presented in Sec. III B, the mean droplet radius is higher for z_e=1380 m than for z_e=1350 m. The size distribution predicted with the two-way coupled model is still broad for both altitudes, so it can be concluded that the phenomena of latent heat release and vapor depletion do not qualitatively affect the spectral broadening. They mainly seem to affect the average size and variance of the droplet size distribution, but not the shape of the distribution function itself.

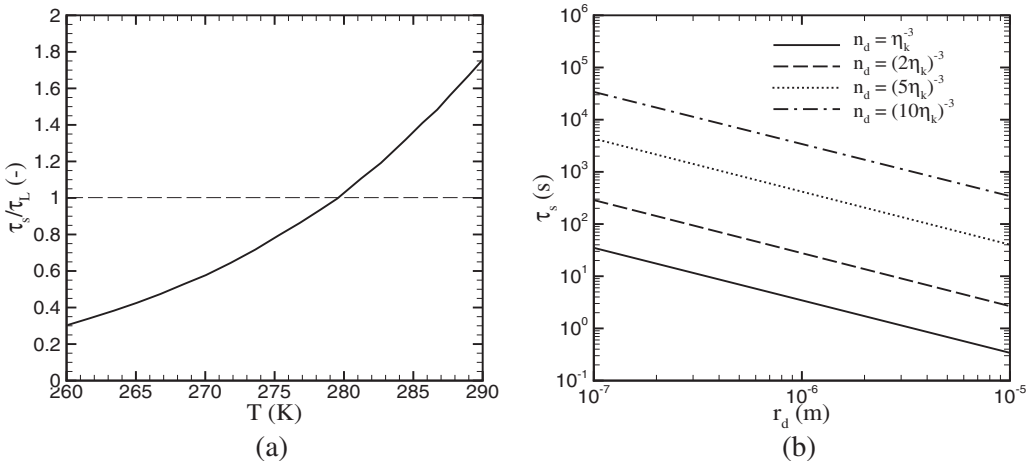

FIG. 12. (a) Ratio between the vapor depletion time scale and the latent heat time scale $\tau_{\mathcal{L}}$, as a function of the temperature T. The partial air density is taken as $\rho_v = 1.2$ kg m^{-3} and the pressure is 10^5 Pa. (b) Vapor depletion time scale τ_s as a function of the droplet radius, for four different values of the droplet number density n_d. The temperature is taken as $T = 280$ K and the pressure as 10^5 Pa. For convenience, the dashed line representing $\tau_s/\tau_{\mathcal{L}} = 1$ is also shown.

We can explain these results in more detail as follows. If the supersaturation is small ($s \ll 1$), Eq. (13) can be rewritten using Eq. (18) to obtain

$$\frac{ds}{dt} \simeq \Gamma \mathbf{u} \cdot \mathbf{e}_z \frac{d}{dT}(\ln \rho_v^s) - s\left(\frac{1}{\tau_s} + \frac{1}{\tau_{\mathcal{L}}}\right), \tag{37}$$

where the time scale associated with the latent heat release $\tau_{\mathcal{L}}$ is equal to

$$\tau_{\mathcal{L}} = \frac{\rho_a C_{p,a}}{4\pi r_d n_d D_{\mathrm{va}} \mathcal{L}} \left(\frac{d\rho_v^s}{dT}\right)^{-1}. \tag{38}$$

Thus, vapor depletion and latent heat release have very similar effects on the supersaturation. Comparison between Eqs. (14) and (38) shows that τ_s and $\tau_{\mathcal{L}}$ are related by

$$\frac{\tau_s}{\tau_{\mathcal{L}}} = \frac{\mathcal{L}}{\rho_a C_{p,a}} \frac{d\rho_v^s}{dT}, \tag{39}$$

which ratio is plotted in Fig. 12(a) as a function of the temperature surrounding the droplet. Apparently, the effect of latent heat is dominant if $T \gtrsim 280$ K, whereas the effect of vapor depletion is more important if $T \lesssim 280$ K.

The actual value of τ_s depends only weakly on the pressure and the temperature through D_{va}, and it can therefore be estimated on the basis of the droplet number density n_d and the droplet radius r_d; the result is plotted in Fig. 12(b). The time scale τ_s is inversely proportional to r_d, and hence the effect of vapor depletion [and thus, also the effects of latent heat release at a given temperature, see Fig. 12(a)] becomes more important as the droplet grows. For instance, at a number density $n_d = (5\eta_k)^{-3}$ and a droplet radius smaller than 5 μm, τ_s is much larger than the time scale in which the condensation process takes place ($L_0/U_0 \sim 100$ s). Therefore the condensation process of droplets with $r_d \lesssim 5$ μm is hardly hampered by vapor depletion and latent heat release, which is confirmed by Figs. 11(a)–11(d).

Figure 12(b) also illustrates the importance of the droplet number density: The higher the number density, the less volume of air/water mixture is available per droplet and the less the droplets are able to grow. This is confirmed by Fig. 13, where we have plotted the droplet distribution function at $z_e = 1350$ m and $t_e = 100$ s for several values of n_d. Indeed, the droplet growth is most impeded for the highest number density considered ($n_d = \eta_k^{-3}$), whereas the graph for $n_d = (10\eta_k)^{-3}$ is only slightly different from the droplet size distribution at $t_e = 100$ s shown in Fig. 4.

Finally, we test the sensitivity of the resulting droplet size distributions to the size of the sampling area L. The droplet size distributions obtained for the two-way coupled model with $n_d = (2\eta_k)^{-3}$ are plotted in Fig. 14 for six different values of L in one realization of the flow field. We see that a broad droplet size distribution is found for $L \geq 10$ m, whereas the variance is much smaller for $L \leq 1$ m. This is different from the results obtained with the simplified model (see Fig. 9), where the variance was observed to be almost equal for all sampling sizes. This difference in behavior between the two-way coupled and the simplified models can be explained by comparing the typical time scale for dispersive motion of droplets to set in (denoted by τ_d) to the condensation time scale τ_s. Droplets that are released in a small sam-

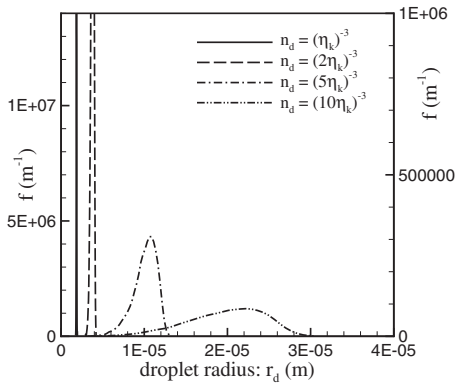

FIG. 13. Droplet radius distribution function $f(r_d)$ at an altitude $z_e = 1350$ m after a time $t_e = 100$ s, for four different droplet number densities. The results have been obtained with the two-way coupled condensation model, with $L^2 = (500\ \mathrm{m})^2$.

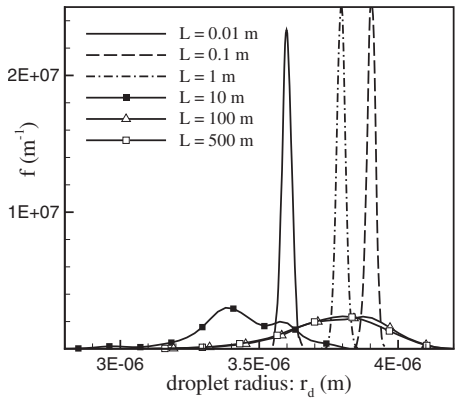

FIG. 14. Droplet radius distribution function $f(r_d)$ at an altitude $z_e=1350$ m after a time $t_e=100$ s, for six different sizes of the sampling area L^2. The results have been obtained with the two-way coupled condensation model, with $n_d=(2\eta_k)^{-3}=1.25\times10^8$ m^{-3}.

pling space and traced backward in time are dispersed to different regions somewhat later than droplets that are released further away from each other [see Fig. 2(b)]. Thus, τ_d is smaller for the latter droplets. As all droplets end up at the same altitude z_e at time $t=t_e$, the dispersive motion takes place during $0<t<t_e-\tau_d$, whereas the influence of vapor depletion effectively sets in for $t>\tau_s$. If $t_e-\tau_d<\tau_s$, the variation in droplet size stems from the dispersive motion through different supersaturation fields. If $t_e-\tau_d>\tau_s$, however, the effect of vapor depletion causes a locally equilibrated size of each droplet regardless of the droplet's origin, which results in a narrower droplet size distribution. This explains why the droplet size distribution is much broader for the larger sampling spaces. Despite this difference in broadening of the droplet size distribution, it may still be concluded that some broadening has occurred for the small sampling spaces, as is observed from Fig. 9, i.e., some spectral broadening also takes place even if the effects of latent heat release and vapor depletion are taken into account.

From the results presented in this section [see Figs. 11(c) and 11(d)] it becomes clear that the droplet size distribution within a fixed sampling area becomes statistically stationary after a sufficiently long time. We can estimate the average size of a group of droplets in this equilibrium situation, $\langle r_d\rangle_{\rm eq}$, by the following heuristic approach. First we reformulate Eq. (37) in an Eulerian frame of reference as

$$\frac{\partial s}{\partial t}+\mathbf{u}\cdot\nabla s=\Gamma\mathbf{u}\cdot\mathbf{e}_z\frac{d}{dT}(\ln\rho_v^s)-s\left(\frac{1}{\tau_s}+\frac{1}{\tau_{\mathcal{L}}}\right). \tag{40}$$

To facilitate further analysis, we assume that $\|\nabla s\| \ll \Gamma d(\ln\rho_v^s)/dT$ so that the convection term can be excluded from Eq. (40). By averaging over all droplets in the sampling area, bearing in mind that both τ_s and $\tau_{\mathcal{L}}$ depend on the droplet size [see Eqs. (14) and (38)], we obtain the following expression:

$$\frac{\partial s}{\partial t}=\Gamma\mathbf{u}\cdot\mathbf{e}_z\frac{d}{dT}(\ln\rho_v^s)-s\left(\left\langle\frac{1}{\tau_s}\right\rangle+\left\langle\frac{1}{\tau_{\mathcal{L}}}\right\rangle\right). \tag{41}$$

If the turbulent velocity fluctuations are accurately described by a Gaussian random noise, we can write Eq. (40) in the form of a stochastic differential equation,[32]

$$ds\simeq -s\left(\left\langle\frac{1}{\tau_s}\right\rangle+\left\langle\frac{1}{\tau_{\mathcal{L}}}\right\rangle\right)dt+\Gamma\frac{d}{dT}(\ln\rho_v^s)\sqrt{2D_z}dW, \tag{42}$$

where dW denotes an increment of a Wiener process, and $D_z\equiv\lim_{t\to\infty}t^{-1}\frac{1}{2}\langle|z(t)-z(0)|^2\rangle$ is the diffusion coefficient of droplets in the vertical direction. Since the flow is statistically isotropic, $D_z=\frac{1}{3}D_{\rm turb}$, where $D_{\rm turb}$ is the three-dimensional diffusion coefficient which can be determined from Fig. 2(a). Equation (42) describes an Ornstein–Uhlenbeck process,[32] for which the steady-state solution of the PDF is a Gaussian distribution with a mean $\bar{s}=0$ and a variance equal to

$$\mathrm{var}(s)=\overline{s^2}=\left(\Gamma\frac{\mathrm{d}}{\mathrm{d}T}(\ln\rho_v^s)\right)^2D_z\left(\left\langle\frac{1}{\tau_s}\right\rangle+\left\langle\frac{1}{\tau_{\mathcal{L}}}\right\rangle\right)^{-1}. \tag{43}$$

It is noted from Eqs. (14) and (38) that $\tau_{\mathcal{L}}$ and τ_s are both inversely proportional to the droplet radius so that $\langle 1/\tau_s\rangle+\langle 1/\tau_{\mathcal{L}}\rangle=\beta\langle r_d\rangle_{\rm eq}$, where $\langle r_d\rangle_{\rm eq}$ is the droplet radius averaged over all droplets situated in the small volume around $\mathbf{x}$, and where the factor β is given by

$$\beta=4\pi D_{\rm va}n_d\left(1+\frac{\mathrm{d}(\rho_v^s)/\mathrm{d}T}{\rho_a C_{pa}}\right). \tag{44}$$

Therefore, Eq. (43) can be rewritten as

$$\langle r_d\rangle_{\rm eq}=(\overline{s^2})^{-1}\left(\frac{\{\Gamma\mathrm{d}(\ln\rho_v^s)/\mathrm{d}T\}^2}{4\pi n_d}\right)\left(\frac{D_z}{D_{\rm va}}\right)\left(1+\frac{\mathrm{d}(\rho_v^s)/\mathrm{d}T}{\rho_a C_{pa}}\right)^{-1}. \tag{45}$$

Thus, we have now found an explicit expression for the average droplet radius in an air parcel located at position $\mathbf{x}$. The expression is valid in the long-time limit in which a statistical equilibrium exists. Equation (45) depends only on the droplet number density n_d, the turbulent diffusion coefficient D_z, the mean-square supersaturation fluctuations $\overline{s^2}$, and the temperature (through $D_{\rm va}$, Γ, $d(\ln\rho_v^s)/dT$, and $\tau_s/\tau_{\mathcal{L}}$). In the flow field employed in the present study, the turbulent diffusion coefficient $D_z\simeq 15$ m^2/s and the rms supersaturation fluctuations are approximately 1%. Using these values, we calculate $\langle r_d\rangle_{\rm eq}$ as a function of temperature for four different values of n_d and plot the result in Fig. 15.

It is observed that the order of magnitude of $\langle r_d\rangle_{\rm eq}$ corresponds reasonably well to the order of magnitude observed in previous graphs. For example, $\langle r_d\rangle_{\rm eq}\simeq 10^{-5}$ m for $n_d=(5\eta_k)^{-3}$ and $T=280$ K, which corresponds to the situation in Fig. 11(a). Since the value of $\langle r_d\rangle_{\rm eq}$ decreases moderately with temperature, it is logical that the eventual droplet radius at higher altitudes [see Fig. 11(d)] is somewhat large than at lower altitudes [see Fig. 11(b)]. More generally, the present analysis suggests that the largest droplets are found in the coolest regions of a cloud.

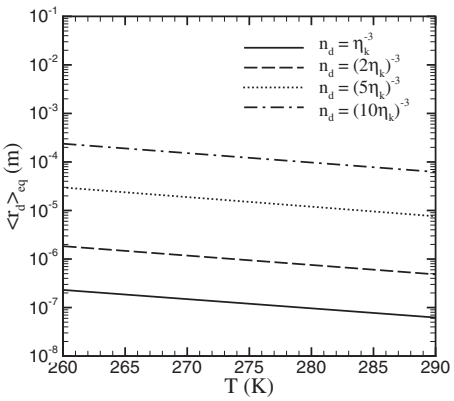

FIG. 15. Long-time value of the average size of droplets in an air parcel $\langle r_d \rangle_{eq}$ as a function of temperature calculated from Eq. (45), for four different values of the droplet number density n_d. We have taken the turbulent diffusion coefficient $D_z = 15$ m^2/s and the rms of the supersaturation $\sqrt{\overline{s^2}} = 1\%$.

The results obtained with the two-way coupled model are qualitatively in agreement with the observations by Celani *et al.*[20] and Lanotte *et al.*:[21] both studies report a broadening of the droplet size distribution, with droplet growth slowing down once a significant fraction of vapor has been absorbed. This agreement is not a surprising outcome since the physics incorporated in the present condensation model is to large extent similar to that employed in Refs. 20 and 21. The main difference between our two-way coupled model and their Eulerian–Lagrangian models, apart from that our model allows for the simulation of all scales in the turbulent spectrum usually present in atmospheric clouds, is that we do not account for exchange of energy and vapor between our droplet/air parcels and the ambient cloud environment. This means that on the one hand, the effects of vapor depletion and latent heat release are overestimated by our two-way coupled model, but on the other hand, our one-way coupled model (simplified model) clearly underestimates these effects. Thus with respect to these influences, the models employed in Refs. 20 and 21 lie somewhere between our one- and two-way coupled models, which explains why there is good qualitative agreement between the predictions. In quantitative sense, a direct comparison is less appropriate not only because certain details of the physics are different, as mentioned above, but also because the initial conditions for the droplet radii are not identical. Celani *et al.*[20] used an initial droplet radius of $r_0 = 4$ μm and Lanotte *et al.*[21] set $r_0 = 5$ μm, whereas the present investigation employs $r_0 = 0.1$ μm. Quantitatively, the initial growth of droplets thus proceeds very differently, but once the feedback effects associated with vapor depletion and latent heat release become significant, the quantitative agreement between the predictions should be more favorable. Indeed, comparing the data reported in Refs. 20 and 21 with the results in Fig. 11(b), we find that the mean droplet sizes are of comparable magnitude [$\mathcal{O}(10$ μm)], with our predicted size variance being slightly smaller than that in Refs. 20 and 21. This can be attributed to the overestimated feedback effect in our two-way coupled model, which results in more uniform supersaturation histories of the droplets.

IV. CONCLUSIONS

In this paper the condensation of microdroplets in atmospheric clouds has been investigated theoretically and numerically. Droplets have been followed through a synthetic turbulent flow field composed of 200 random Fourier modes, with wave numbers ranging from the integral scale [$\mathcal{O}(10^2$ m)] to the Kolmogorov scale [$\mathcal{O}(10^{-3}$ m)]. Two fully Lagrangian droplet growth models have been developed: a two-way coupled model which includes adiabatic cooling, vapor depletion, and latent heat, and a simplified model where the latter two are neglected.

The simulations with the simplified model demonstrate that the droplet size distribution becomes broader in the course of time. At higher altitudes, the mean radius of droplets is larger than at low altitudes and the number of droplets evaporating decreases. We show analytically that the PDF of the droplet surface Σ_d is related to the turbulent dispersion of droplets and becomes broader in the course of time. At altitudes where the supersaturation is close to zero, the PDF of Σ_d is positively skewed due to the effect of droplet evaporation, whereas the PDF of the droplet radius is very similar to a Gaussian distribution.

By testing different ranges of wavemodes, it is illustrated that the spectral broadening on centimeter scales is caused by both large scales of turbulence and small scales: large scales transport droplets through regions of different supersaturations, whereas small scales mix droplets of different sizes.

While the simplified condensation model neglects vapor depletion and latent heat release, their effects are slightly overestimated in the two-way coupled condensation model, as we have neglected mechanisms such as diffusion, which allow the parcel to exchange water vapor and thermal energy with its surroundings. Nonetheless the results for the droplet size distributions obtained with the two-way coupled model are qualitatively similar to the results from the simplified model, in the sense that broad droplet size distributions are found for droplets with radius $r_d \simeq 10$ μm. Quantitatively, the droplet sizes obtained are smaller than in the simplified model, and the droplet size distribution in the two-way coupled case reaches a more narrow equilibrium shape after a long time. The results have been explained by determining typical time scales for the vapor depletion τ_s and for the latent heat release $\tau_{\mathcal{L}}$. $\tau_{\mathcal{L}}$ is shown to be smaller than τ_s for high temperatures $T \gtrsim 280$ K so that latent heat release is dominant over vapor depletion in this regime. Vice versa, vapor depletion is more important than latent heat for $T \lesssim 280$ K. Since τ_s and $\tau_{\mathcal{L}}$ are inversely proportional to the droplet radius r_d, both effects become more important as the droplet radius grows. This is the reason why an equilibrium is reached when the droplets have become sufficiently large. The average droplet size in the equilibrium situation is of the order of 10 μm for a realistic value of the droplet number density n_d such as $(2\eta_k)^{-1}$.[18]

To conclude, the present results demonstrate that the condensation process in turbulent flow representative for atmospheric clouds leads to a broad droplet size distribution within volumes comparable to the smallest scales of the turbulent flow. This phenomenon is likely to be an essential

ingredient in the rapid growth of droplets due to coalescence in a subsequent stage of rain formation.

Although the approach in this study is specifically aimed at predicting droplet condensation in atmospheric clouds, it could be of importance in other turbulent flows with condensation as well, especially if the condensation takes place nonhomogeneously and if the time scales of the condensation process are comparable to the time scales of turbulent mixing.

ACKNOWLEDGMENTS

R.S.R.S. thanks the Institute of Mechanics, Processes and Control-Twente (IMPACT) at the University of Twente for the financial support to the Spearhead Program on Dispersed Multi-phase Flows. R.H.A.I.J. gratefully acknowledges the financial support from EPSRC (U.K.), Contract No. EP/E029973/1.

APPENDIX A: SELECTION OF COEFFICIENTS IN KINEMATIC SIMULATION OF FLOW FIELD

In this appendix we describe how the random coefficients $\mathbf{k}_n$, $\mathbf{A}_n$, $\mathbf{B}_n$, and ω_n that appear in Eq. (2) are selected. The wave vectors $\mathbf{k}_n$ are chosen such that the following model energy spectrum[33] is approximately satisfied,

$$E(k) = \alpha k^{-5/3} f_L(kL) f_\eta(k\eta_k), \quad k_1 \le k \le k_N,$$

$$E(k) = 0, \quad \text{otherwise},$$

where $k \equiv \|\mathbf{k}\|$, and L_0 denotes the integral length scale. The function $f_L(kL_0)$ is a correction to the standard $-5/3$-spectrum that incorporates the contribution of the largest scales of motion, and is given by

$$f_L(kL_0) = \left[\frac{kL_0}{\sqrt{(kL_0)^2 + C_L}}\right]^{5/3+p_0}, \tag{A1}$$

with $C_L = 6.78$ and $p_0 = 2$. Similarly, the function $f_\eta(k\eta_k)$ incorporates the contribution of the eddies in the dissipative range, and is given by

$$f_\eta(k\eta_k) = \exp(-\beta\{[(k\eta_k)^4 + C_\eta^4]^{1/4} - C_\eta\}), \tag{A2}$$

with $C_\eta = 0.40$ and $\beta = 5.2$. The factor α contained in the energy spectrum is related to the energy dissipation rate ϵ by $\alpha \propto \epsilon^{2/3}$, and is obtained from the condition

$$\int_0^\infty E(k)dk = \frac{3}{2}U_0^2, \tag{A3}$$

where U_0 is a specified reference velocity. Figure 1 shows the energy spectrum that is used to generate the velocity field in the present investigation.

The norms $k_n \equiv \|\mathbf{k}_n\|$ are distributed in logarithmic fashion between the wave numbers associated with the maximum length scale $L_{\max}$ and the Kolmogorov length scale η_k,

$$k_1 = \frac{2\pi}{L_{\max}}, \quad k_N = \frac{2\pi}{\eta_k}, \quad k_n = k_1\left(\frac{k_N}{k_1}\right)^{(n-1)/(N-1)} \quad \text{for } 1 < n < N. \tag{A4}$$

The maximum length scale $L_{\max}$ should be larger than L_0, and its value is set equal to $5L_0$ in this study. The wave numbers $\mathbf{k}_n$ are determined by setting $\mathbf{k}_n = k_n\mathbf{e}_n$, where $\mathbf{e}_n$ is a unit vector whose direction is randomly chosen. This is achieved by taking $\mathbf{e}_n = (\sqrt{1-h^2}\cos\theta, \sqrt{1-h^2}\sin\theta, h)^T$, where the variables h and θ are randomly sampled from the respective domains $[-1,1]$ and $[0,2\pi]$ based on a uniform probability distribution. In order to ensure that the velocity field satisfies the energy spectrum, the norms of the amplitude coefficients $\mathbf{A}_n$ and $\mathbf{B}_n$ are determined from

$$\|\mathbf{A}_n\|^2 = \|\mathbf{B}_n\|^2 = 2\int_{k_{n-1/2}}^{k_{n+1/2}} E(k)dk, \tag{A5}$$

where $k_{n\pm1/2} = (k_n + k_{n\pm1})/2$. The direction of $\mathbf{A}_n$ is specified by setting $\mathbf{A}_n = \|\mathbf{A}_n\|\mathbf{a}_n$; the unit vector $\mathbf{a}_n$ has a random direction in a plane which is orthogonal to $\mathbf{k}_n$, and is calculated by

$$\mathbf{a}_n = \frac{\mathbf{t}_n \times \mathbf{k}_n}{\|\mathbf{t}_n \times \mathbf{k}_n\|}, \tag{A6}$$

where the randomly directed unit vector $\mathbf{t}_n$ is determined in a similar fashion as $\mathbf{e}_n$. Determination of the amplitude coefficients $\mathbf{B}_n$ proceeds in a similar way as outlined for $\mathbf{A}_n$.

The velocity field is completed by specifying the angular frequencies ω_n, which are chosen to be proportional to the eddy-turnover time associated with the nth Fourier mode,[34]

$$\omega_n = \lambda\sqrt{k_n^3 E(k_n)}, \tag{A7}$$

where λ is the so-called unsteadiness parameter, which is generally taken to be $0 \le \lambda \le 1$. In this investigation its value is set to unity: $\lambda = 1$. Other values of λ (i.e., $\lambda = 0.1$ and $\lambda = 0.5$) have been tested as well, but they did not alter the dispersion statistics of the resulting flow field qualitatively.

APPENDIX B: LIQUID PROPERTIES AND CONSTANTS

In this appendix, the material properties that have been used in the present research are summarized. The specific heat capacities for dry air are[4] $C_{p,a} = 1004.0$ J kg^{-1} K^{-1} and $C_{v,a} = 716.96$ J kg^{-1} K^{-1}. The gas constant thus becomes $R_a = C_{p,a} - C_{v,a} = 287.04$ J kg^{-1} K^{-1}. The specific latent heat $\mathcal{L}$ is a function of the temperature of the evaporating liquid. For water at temperatures between 200 K $< T <$ 300 K it can be approximated by[4]

$$\mathcal{L} = A_{\mathcal{L},0} + A_{\mathcal{L},1}T \tag{B1}$$

with

$$A_{\mathcal{L},0} = 3\,105\,913.39 \text{ J kg}^{-1}$$

and

$$A_{\mathcal{L},1} = -2212.97 \text{ J kg}^{-1}\text{ K}^{-1}.$$

The saturation vapor density $\rho_v^s(T)$ can be determined from[35]

$$\rho_v^s = \frac{p_s}{(C_{p,v} - C_{v,v})T}, \tag{B2}$$

where $p_s(T)$ is the saturation vapor density given by

$$p_s = \exp\left(A_{p,1} + A_{p,2}T + A_{p,3}T^2 + A_{p,4}\ln(T) + \frac{A_{p,5}}{T}\right), \quad \text{(B3)}$$

with $A_{p,1}=21.125$, $A_{p,2}=-2.7246\times10^{-2}$, $A_{p,3}=1.6853\times10^{-5}$, $A_{p,4}=2.4576$, and $A_{p,5}=-6094.4642$.

The binary diffusion coefficient D_{va} is a function of temperature and pressure. The temperature is determined from Eq. (18), while the pressure can be obtained from the air density ρ_a and the temperature using the equation of state: $p=\rho_a R_a T$. The expression for D_{va} is given by[27]

$$D_{va} = \frac{2.49}{p}\left(\frac{T}{295}\right)^{1.75}. \quad \text{(B4)}$$

[1] R. A. Shaw, "Particle-turbulence interactions in atmospheric clouds," Annu. Rev. Fluid Mech. **35**, 183 (2003).
[2] J.-L. Brenguier and L. Chaumat, "Droplet spectra broadening in cumulus clouds. Part I: Broadening in adiabatic cores," J. Atmos. Sci. **58**, 628 (2001).
[3] L. Chaumat and J.-L. Brenguier, "Droplet spectra broadening in cumulus clouds. Part II: Microscale droplet concentration heterogeneities," J. Atmos. Sci. **58**, 642 (2001).
[4] H. R. Pruppacher and J. D. Klett, *Microphysics of Clouds and Precipitation* (Reidel, Dordrecht, Holland, 1980).
[5] J. H. Seinfeld and S. N. Pandis, *Atmospheric Chemistry and Physics: From Air Pollution to Climate Change*, 2nd ed. (Wiley, New Jersey, 2006).
[6] A. Celani, A. Mazzino, and M. Tizzi, "The equivalent size of cloud condensation nuclei," New J. Phys. **10**, 075021 (2008).
[7] K. D. Squires and J. K. Eaton, "Preferential concentration of particles by turbulence," Phys. Fluids A **3**, 1169 (1991).
[8] S. Goto and J. C. Vassilicos, "Self-similar clustering of inertial particles and zero-acceleration points in fully developed two-dimensional turbulence," Phys. Fluids **18**, 115103 (2006).
[9] R. H. A. IJzermans, M. W. Reeks, E. Meneguz, M. Picciotto, and A. Soldati, "Measuring segregation of inertial particles in turbulence by a full Lagrangian approach," Phys. Rev. E **80**, 015302(R) (2009).
[10] M. Wilkinson, B. Mehlig, S. Östlund, and K. P. Duncan, "Unmixing in random flows," Phys. Fluids **19**, 113303 (2007).
[11] M. R. Maxey, "The gravitational settling of aerosol particles in homogeneous turbulence and random flow fields," J. Fluid Mech. **174**, 441 (1987).
[12] C. Pasquero, A. Provenzale, and E. A. Spiegel, "Suspension and fall of heavy particles in random two-dimensional flow," Phys. Rev. Lett. **91**, 054502 (2003).
[13] C. T. Crowe, J. N. Chung, and T. R. Troutt, *Particulate Two-Phase Flow* (Heinemann, Oxford, 1993).
[14] J. Bec, A. Celani, M. Cencini, and S. Musacchio, "Clustering and collisions of heavy particles in random smooth flows," Phys. Fluids **17**, 073301 (2005).
[15] S. Twomey, "The nuclei of natural cloud formation. Part II: The supersaturation in natural clouds and the variation of cloud droplet concentration," Geofis. Pura Appl. **43**, 243 (1959).
[16] K. V. Beard and H. T. J. Ochs, "Warm-rain initiation: An overview of microphysical mechanisms," J. Appl. Meteorol. **32**, 608 (1993).
[17] P. A. Vaillancourt, M. K. Yau, and W. W. Grabowski, "Microscopic approach to cloud droplet growth by condensation. Part I: Model description and results without turbulence," J. Atmos. Sci. **58**, 1945 (2001).
[18] P. A. Vaillancourt, M. K. Yau, P. Bartello, and W. W. Grabowski, "Microscopic approach to cloud droplet growth by condensation. Part II: Turbulence, clustering, and condensational growth," J. Atmos. Sci. **59**, 3421 (2002).
[19] A. Celani, G. Falkovich, A. Mazzino, and A. Seminara, "Droplet condensation in turbulent flows," Europhys. Lett. **70**, 775 (2005).
[20] A. Celani, A. Mazzino, A. Seminara and M. Tizzi, "Droplet condensation in two-dimensional Bolgiano turbulence," J. Turbul. **8**, 17 (2007).
[21] A. S. Lanotte, A. Seminara, and F. Toschi, "Cloud droplet growth by condensation in homogeneous isotropic turbulence," J. Atmos. Sci. **66**, 1685 (2009).
[22] B. A. van Haarlem, "The dynamics of particles and droplets in atmospheric turbulence," Ph.D. thesis, Delft University of Technology, 2000.
[23] M. Andrejczuk, W. W. Grabowski, S. P. Malinowski, and P. K. Smolarkiewicz, "Numerical simulation of cloud-clear air interfacial mixing," J. Atmos. Sci. **61**, 1726 (2004).
[24] R. H. Kraichnan, "Diffusion by a random velocity field," Phys. Fluids **13**, 22 (1970).
[25] F. Nicolleau and G. Yu, "Two-particle diffusion and locality assumption," Phys. Fluids **16**, 2309 (2004).
[26] D. R. Osborne, J. C. Vassilicos, K. Sung, and J. D. Haigh, "Two-particle diffusion and locality assumption," Phys. Rev. E **74**, 036309 (2006).
[27] G. Lamanna, "On nucleation and droplet growth in condensing nozzle flows," Ph.D. thesis, Eindhoven University of Technology, 2000.
[28] Y. S. Sedunov, *Physics of Drop Formation in the Atmosphere* (Wiley, New York, 1974).
[29] G. I. Taylor, "Diffusion by continuous movements," Annu. Rev. Fluid Mech. **20**, 196 (1921).
[30] L. F. Richardson, ""Atmospheric diffusion shown on a distance-neighbour graph," Proc. R. Soc. London, Ser. A. **110**, 709 (1926).
[31] D. J. Thomson and B. J. Devenish, "Particle pair separation in kinematic simulations," J. Fluid Mech. **526**, 277 (2005).
[32] N. G. van Kampen, *Stochastic Processes in Chemistry and Physics* (Elsevier, New York, 1992).
[33] S. B. Pope, *Turbulent Flows* (Cambridge University Press, Cambridge, 2000).
[34] J. C. H. Fung and J. C. Vassilicos, "Two-particle dispersion in turbulent-like flows," Phys. Rev. E **57**, 1677 (1998).
[35] F. Put, "Numerical simulation of condensation in transonic nozzle flows," Ph.D. thesis, University of Twente, 2003.